Article

Effects of Transition Metal Substituents on Interfacial and Electronic Structure of CH$_3$NH$_3$PbI$_3$/TiO$_2$ Interface: A First-Principles Comparative Study

Yao Guo [1,2,*], **Yuanbin Xue** [1], **Xianchang Li** [2], **Chengbo Li** [2], **Haixiang Song** [1], **Yongsheng Niu** [1,*], **Hu Liu** [3,4], **Xianmin Mai** [5], **Jiaoxia Zhang** [6] **and Zhanhu Guo** [3,*]

[1] Department of Chemical and Environmental Engineering, Anyang Institute of Technology, Anyang 455000, China
[2] Department of Mathematics and Physics, Anyang Institute of Technology, Anyang 455000, China
[3] Integrated Composites Laboratory (ICL), Department of Chemical & Biomolecular Engineering, University of Tennessee, Knoxville, TN 37996, USA
[4] Key Laboratory of Materials Processing and Mold (Zhengzhou University), Ministry of Education; National Engineering Research Center for Advanced Polymer Processing Technology, Zhengzhou University, Zhengzhou 450002, China
[5] School of Urban Planning and Architecture, Southwest Minzu University, Chengdu 610041, China
[6] School of Material Science and Engineering, Jiangsu University of Science and Technology, Zhenjiang 212003, China
* Correspondence: guoyao@ayit.edu.cn (Y.G.); niuyongsheng@ayit.edu.cn (Y.N.); zguo10@utk.edu (Z.G.)

check for updates

Abstract: To evaluate the influence of transition metal substituents on the characteristics of CH$_3$NH$_3$PbI$_3$/TiO$_2$, we investigated the geometrical and electronic properties of transition metal-substituted CH$_3$NH$_3$PbI$_3$/TiO$_2$ by first-principles calculations. The results suggested that the substitution of Ti^{4+} at the five-fold coordinated (Ti$_{5c}$) sites by transition metals is energetically favored. The substituted interface has enhanced visible light sensitivity and photoelectrocatalytic activity by reducing the transition energies. The transition metal substitution can effectively tune the band gap of the interface, which significantly improves the photo-reactivity. The substituted systems are expected to be more efficient in separating the photo-generated electrons-holes and active in the visible spectrum.

Keywords: organic-inorganic perovskites; interface; first-principles calculations

---

1. Introduction

Hybrid halide perovskites as light harvesters have been the focus of the photovoltaic field over the past years owing to their impressive power conversion efficiency (PCE) and promising commercial applications [1,2]. The CH$_3$NH$_3$PbI$_3$ perovskites dominate this field and have been studied extensively [3]. The typical device architecture of perovskite solar cells (PSC) is composed of the TiO$_2$-based electron transport layer (ETL), the perovskite (CH$_3$NH$_3$PbI$_3$) absorber-based layer, the spiro-OMeTAD hole transport layer (HTL) and the corresponding electrodes [4]. The perovskite/ETL interface plays an important role in determining the charge separation and transport properties as well as the PSC device performance, which has been widely explored for many years [5–8].

TiO$_2$ is a good candidate material due to its chemical stability, high charge transport property and low cost [9]. The electron can be effectively transported from CH$_3$NH$_3$PbI$_3$ to the TiO$_2$ layer because the conduction band of TiO$_2$ is lower than that of CH$_3$NH$_3$PbI$_3$ [10]. Generally, the ultra-thin compact TiO$_2$ layer is prepared at a high temperature (over 450 °C) [11]. It seriously undermines

the electrical properties of the ETL in conductivity, mobility, and electronic trap states, thereby affecting the efficiency and stability of PSC. Elemental substitution in the compact TiO_2 layer is an effective solution to improve the electrical properties and device performance [12–21]. Transition metal substitution [22] is an effective approach to enhance the photocatalytic activity of TiO_2 due to their unique *d* electronic configuration and spectral characteristics. According to previous studies [13–21], a wide range of substitutional elements such as Zn^{2+}, Y^{3+}, Nb^{5+}, Ru^{4+} and W^{6+} have been investigated in TiO_2. Research has made remarkable progress in identifying that the substitution of the TiO_2 layer by the transition metal in PSC is an effective mean to improve the photocurrent and electron-hole recombination [14–18]. Substituents in TiO_2 film can improve the electrical characteristics of ETL, which promote PCE and stability of PSC [13,23]. Therefore, transition metal substituents in the TiO_2 layer are quite important and further characterizations are required to understand the effects of substituents in the $CH_3NH_3PbI_3/TiO_2$ interface. Although the electronic properties of perovskite/ETL interface have been widely investigated by experiments and density-functional-theory (DFT) calculations [24–31], the existence of theoretical studies aiming to understand the fundamental role of the interfacial substituents is still rather scarce. In addition to the primary experiments, the first-principles DFT calculations are highly important to acquire further knowledge concerning the effects of transition metal substitution and contribute to new strategies for interface optimization. The main contributions of our study are helpful to draw guidelines for substitution mechanism of the $CH_3NH_3PbI_3/TiO_2$ interface, thus enhancing the photovoltaic performance in PSC.

2. Methods

The Vienna *ab initio* simulation package (VASP) [32] was employed as the first-principles calculations platform. The computer software program is based on the DFT approach using plane wave basis within a periodic boundary condition. The projected augmented wave (PAW) [33] pseudopotentials were applied for efficient computation. The exchange and correlations items were treated within the framework of generalized-gradient approximation (GGA) of Perdew-Burke-Ernzerhof (PBE) [34]. A plane wave basis cutoff energy of 500 eV was used. Integrations in reciprocal space were sampled using the Monkhorst-Pack grids [35] with a minimum spacing of 0.2 Å^{-1}. Convergence criteria were set as 1.0^{-6} eV in total energy and 1.0^{-2} eV/Å in atomic force, respectively. Recent theoretical studies indicated that the *GW* (Green's function *G* with screened interaction *W*) and hybrid functional approach can provide an accurate description of the electronic structures [36,37]. Fortunately, DFT was able to qualitatively reproduce the *GW* trend. Hence, we performed GGA+*U* calculations on the $CH_3NH_3PbI_3/TiO_2$ interfaces with reasonable computational cost. Based on previous research and experiences [38–43], the GGA+*U* approach with the on-site Coulomb interaction correction predicted band gap correctly. The values of parameter *U* were 6 eV for the Ti^{4+} 3*d* orbit and 4 eV for the *d*-orbits of transition metal substituents. Gaussian broadening [44] with half-width of 0.1 eV for the electronic eigenvalues was used to accelerate the convergence in the *k*-point sum. The dipole correction was included because the interface configuration does not have mirror symmetry along the *c*-axis. The spin orbit coupling (SOC) effect [45] was not included because it was negligible in the geometry. The atomic structures shown were produced by using the visualization for electronic and structural analysis (VESTA) program [46].

According to the experimental results [47], there is an ordered lattice structure existing on the $CH_3NH_3PbI_3/TiO_2$ interface. The (110) slab of the $CH_3NH_3PbI_3$ nanocrystal coordinated with the (101) slab of anatase TiO_2, forming an ordered lattice structure at the interface. The lattice mismatch between $CH_3NH_3PbI_3$ (110) and TiO_2 (101) has been evaluated in previous studies [48]. It was found that using the experimental results of the $CH_3NH_3PbI_3$ (110) surface, the band-gap only varies slightly, with a corresponding total energy decrease, suggesting that a minimal strain is introduced by the lattice mismatch between the two materials. In spite of a relatively large lattice mismatch, we selected the experimental interface [47] between $CH_3NH_3PbI_3$ (110) and TiO_2 (101) to carry out the investigation. To construct the aspired interface structures, the $CH_3NH_3PbI_3$ (110)/TiO_2 (101) interface was chosen as our objective due to the experimental results [47] and stability of the corresponding surface. The (2×2) supercell of the $CH_3NH_3PbI_3$ (110) and the (1×3) supercell of the anatase TiO_2 (101) were employed to decrease the misfit. The interface model employed the average size of both $CH_3NH_3PbI_3$ and TiO_2 slabs to make a small mismatch. The $CH_3NH_3PbI_3$ perovskite was composed of the CH_3NH_3I and PbI_2 units along the [001] direction; therefore, both CH_3NH_3I and PbI_2 terminations using five-layer slabs were considered in this work. The anatase (101) supercell contains 36 TiO_2 units or 108 substrate atoms. The interfaces were built by connecting the $CH_3NH_3PbI_3$ (110) slab with the anatase (101) slab and leaving a 20 Å vacuum gap in the perpendicular direction. A schematic representation of the interfacial system used in this work is presented in Figure 1. In fact, the TiO_2 was the substrate to grow perovskite films; hence, apart from the bottom two Ti and four O layers, which were maintained in their ideal bulk positions, all atomic coordinates of the others layers were fully relaxed. The transition metal-substituted anatase (101) surface model was constructed by substituting the surface Ti^{4+} with substituent atoms. As shown in Figure 2, there are two possible surface sites (five/six-fold coordinated Ti^{4+} cation, hereafter abbreviated as Ti_{5C} and Ti_{6C}) for the substituent atoms to replace [49]. Till date, the atomic arrangement of the $CH_3NH_3PbI_3/TiO_2$ is still unclear due to limit of the experimental techniques. Based on previous studies of the transition metal-substituted TiO_2 surface [50,51], the interfacial configurations were carefully designed to make the substituent effect more prominent at the interface region. We assume that all six different transition metal ions partially substituted at the Ti^{4+} sites (Ti_{5C} or Ti_{6C}) correspond to the substitution concentration of 17% and the supercell is represented by $Ti_{0.83}M_{0.17}O_2$ ($M = Zn^{2+}, Y^{3+}, Zr^{4+}, Nb^{5+}, Ru^{4+}, W^{6+}$). The substituents can be classified as $3d$ transition metal (Zn^{2+}), $4d$ transition metal ($Y^{3+}, Zr^{4+}, Nb^{4+}, Ru^{4+}$) and $5d$ transition metal (W^{6+}) ions.
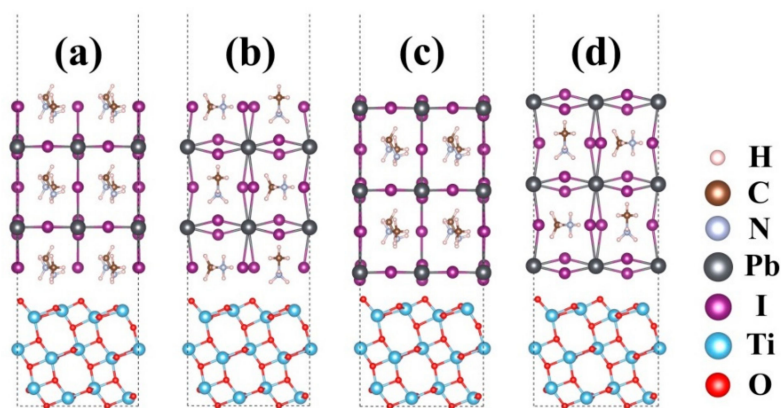

Figure 1. Schematic illustration of pristine $CH_3NH_3PbI_3/TiO_2$ interface models: (**a**) CH_3NH_3I/TiO_2 (**b**) CH_3NH_3I/TiO_2 with rotation (**c**) PbI_2/TiO_2 (**d**) PbI_2/TiO_2 with rotation.

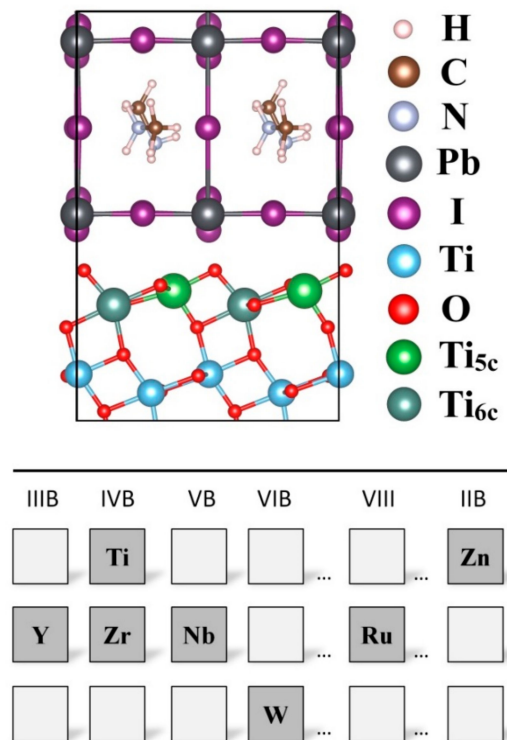**Figure 2.** Schematic illustration of the transition metal substituents at Ti_{5C} and Ti_{6C} sites of the $CH_3NH_3PbI_3/TiO_2$ interface.

3. Results and Discussions

As shown in Table 1, the optimized 0 K DFT lattice parameters of anatase TiO_2 crystal are $a = 3.79$ Å and $c = 9.53$ Å, which is in agreement with previous experiments [52]. The atomic positions of tetragonal $CH_3NH_3PbI_3$ are based on the results of the previous report [53,54]. The 0 K DFT lattice parameters are $a = 8.80$ Å and $c = 13.05$ Å. The strong interfacial interaction in $CH_3NH_3PbI_3/TiO_2$ is mainly through iodine and under-coordinated titanium atoms. The stability of the selected interface can be evaluated by comparing the calculated binding energies [55,56]. The calculated binding energies of different interfaces are listed in Table 2, together with lattice mismatch. The lattice mismatch between $CH_3NH_3PbI_3$ and TiO_2 was −12.0% and −13.8%, respectively. The interfacial binding energies and lattice mismatch can be predicted by the following equations [25]:

$$E_{\text{binding}} = E_{\text{anatase}} + E_{\text{perovskite}} - E_{\text{total}} \tag{1}$$

$$M_{perovskite/anatase} = (a_{perovskite} - a_{anatase})/a_{perovskite} \tag{2}$$

where E_{total}, E_{anatase}, and $E_{\text{perovskite}}$ are the corresponding energies of the interface, anatase and perovskite surfaces, respectively. The $a_{anatase}$ and $a_{perovskite}$ represent the lattice parameter of TiO_2 and $CH_3NH_3PbI_3$, respectively. Zero energy corresponds to the energetically less-stable structure. It is not surprising that the perovskite/TiO_2 interfaces without rotation are more stable than their corresponding rotated ones. This could be because of the difference in lattice mismatches. The strain may affect the interfacial stability between perovskite and TiO_2. For rotation-free interfaces, the E_{binding} of the two systems is quite similar. The $CH_3NH_3^+$ cation interacted with TiO_2 partially containing weak van der Waals (vdW) interactions. In contrast, the interaction between Pb^{2+} cation and TiO_2 leads to the formation of stable chemical bonds. This character is similar to previous works [25,54]. The interfacial structures of the relatively stable rotation-free perovskite/TiO_2 are adopted in subsequent calculations. The interface supercell lattice parameters are given by $a = 10.95$ Å, $b = 11.64$ Å and $c = 49.95$ Å.

Table 1. Calculated lattice parameters of TiO$_2$ and MAPbI$_3$ and deviation between experiment and simulation.

	Anatase TiO$_2$		Tetragonal -MAPbI$_3$	
	a	*c*	*a*	*c*
Experimental	3.785	9.514	8.80	12.685
Calculated	3.79	9.53	8.80	13.05
Deviation	0.13%	0.17%	-	2.8%

Table 2. Interfacial binding energy (in eV) and lattice mismatch of the CH$_3$NH$_3$PbI$_3$/TiO$_2$ interfaces.

	CH$_3$NH$_3$I/TiO$_2$	PbI$_2$/TiO$_2$	CH$_3$NH$_3$I/TiO$_2$ With Rotation	PbI$_2$/TiO$_2$ With Rotation
Binding energy	2.16	2.07	0.00	1.44
Lattice mismatch	−12.0%	−12.0%	−13.8%	−13.8%
Charge transfer	−0.29	−0.28	−0.16	−0.16

To explore the influence of transition metal substitution on the interfacial stability of the CH$_3$NH$_3$PbI$_3$/TiO$_2$ interface structure, the Nb-substituted interfaces were systematically investigated. The dependence of Nb^{5+} substituent on the depth within the interface layers were evaluated based on the total energies (seen Table 3). The six-coordinated Ti$_{6C}$ substituted interface with the lowest total energy is accepted as the most stable configuration. Despite the cleaved and unsaturated bond, the five-coordinated Ti$_{5C}$ substituted interfaces still show relative low total energy. The Nb^{5+} substituent was energetically favorable at the Ti$_{5C}$ and Ti$_{6C}$ sites of the TiO$_2$ surface. Therefore, to characterize the effect of substitution at the CH$_3$NH$_3$PbI$_3$/TiO$_2$ interface, both Ti$_{5C}$ and Ti$_{6C}$ substitution sites are considered in subsequent calculations. The substitution of Nb^{5+} at both Ti$_{5C}$ site and Ti$_{6C}$ sites in the top TiO$_2$ layer was considered. For each situation, two different configurations, namely CH$_3$NH$_3$I/TiO$_2$ and PbI$_2$/TiO$_2$, were considered in this study. The calculated interfacial binding energies and Bader charge were listed in Table 4. The interfacial binding energies become stronger after substitution, which indicates that substituting Ti^{4+} with Nb^{5+} could enhance the stability and strength of the perovskite/TiO$_2$ interface. The CH$_3$NH$_3$I/TiO$_2$ interface has a larger energy than the PbI$_2$/TiO$_2$ interface. The degree of charge transferring is evaluated by the Bader charge analysis [57]. The negative value means the transfer of excess electrons from the perovskite to TiO$_2$ because the perovskite layer has a higher average potential than the TiO$_2$ layer. As can be seen in Table 4, there is less charge transfer in the PbI$_2$/TiO$_2$ than that of the CH$_3$NH$_3$I/TiO$_2$. This can be explained by the fact that the PbI$_2$ layers have a relatively lower potential than the CH$_3$NH$_3$I layers. Moreover, it also can be seen that the Nb^{5+} substituents located at the Ti$_{5C}$ site have a larger charge transfer than that of the Ti$_{6C}$ site. Liu et al. reported that the potential drop on the CH$_3$NH$_3$I/TiO$_2$ is deeper than that of the PbI$_2$/TiO$_2$ [25]. As a result, a strong accumulation region can be formed at the CH$_3$NH$_3$PbI$_3$/TiO$_2$ interface, leading to a better electron-hole separation in the PSC. To emphasize and compare the influence of more different transition metal substituents on the CH$_3$NH$_3$PbI$_3$/TiO$_2$ interface, we make the approximation that only the Ti$_{5C}$-substitute interface will be considered in subsequent investigations.

**Table 3.** Total energy (in eV) of CH$_3$NH$_3$PbI$_3$/TiO$_2$ with substitution of one Nb^{5+} for Ti^{4+}.

Position	Surface (Ti$_{5c}$)	Sub-Surface (Ti$_{6c}$)	Inner-Surface (Third Ti Layer)	Inner-Surface (Fourth Ti Layer)
Total energy	−1401.71	−1401.94	−1401.52	−1401.72

Table 4. Interfacial binding energy (in eV) of the Nb-substituted and pristine $CH_3NH_3PbI_3/TiO_2$ interfaces.

	Ti_{5c} Site		Ti_{6c} Site		CH_3NH_3I/TiO_2	PbI_2/TiO_2
	CH_3NH_3I/TiO_2	PbI_2/TiO_2	CH_3NH_3I/TiO_2	PbI_2/TiO_2		
Binding energy	3.59	3.05	2.77	2.54	0.09	0.00
Charge transfer	−0.44	−0.28	−0.26	−0.15	−0.29	−0.28

Both the interfacial charge transfers and $E_{binding}$ of the transition metal-substituted $CH_3NH_3PbI_3/TiO_2$ interfaces in Figure 3 were combined to evaluate the influence of transition metal substitution in the PSC. Transition metals can be divided into three types: n (Nb^{5+}, W^{6+}), p (Zn^{2+}, Y^{3+}) and isovalent (Zr^{4+}, Ru^{4+}) substitutions. Zero energy (pristine) corresponds to the energetically less-stable structure. It can be seen that the transition metals have different $E_{binding}$ while the values of each substituted interface are positive. It also can be discerned clearly from Figure 3 that the transition metal-substituted interface has a much higher binding energy. This suggests that substituting transition metals M ($M = Zn^{2+}$, Y^{3+}, Zr^{4+}, Nb^{5+}, Ru^{4+}, W^{6+}) for Ti^{4+} at the interface layer could significantly enhance the interface strength between perovskite and TiO_2. In addition, Figure 3 displays the comparison of charge transfers at the perovskite/TiO_2 interface substituted with various transition metals. One can clearly see that the charge transfer in the interface becomes larger with the addition of transition metals. It should be pointed out that Zn^{2+} and Y^{3+} substitution for Ti^{4+} at the interface layer is energetically favorable in terms of binding energy (16.6 and 13.5 eV) and charge transfer (−5.8 and −3.1 e) for the PbI_2/TiO_2 interface. This enhancement can be attributed to the optimized energy band alignment, which could improve the electron transfer behavior between ETL and perovskite. The theoretical results can provide support for future experimental design and synthesis of a stable perovskite/TiO_2 interface, possessing strong electron transfer capacity. Due to their relatively stronger binding energies, the interfacial structure of PbI_2/TiO_2 is selected for subsequent investigations.
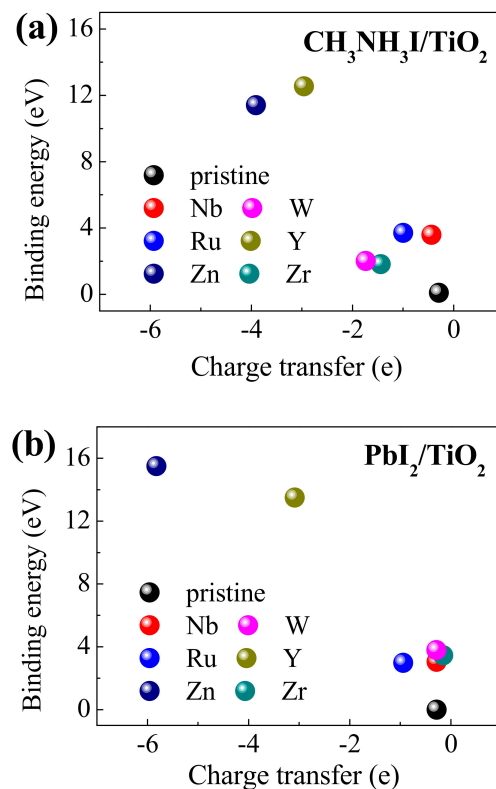
Figure 3. Relationship between the interfacial charge transfers and binding energies of transition metal-substituted $CH_3NH_3PbI_3/TiO_2$: (**a**) CH_3NH_3I/TiO_2 (**b**) PbI_2/TiO_2.

The degree of the total potential drop across the $CH_3NH_3PbI_3/TiO_2$ interfaces reliably indicates their photo-excited charge separation capabilities [58]. To clearly show their difference, the planar averaged electrostatic potential of the seven perovskite/TiO_2 heterostructures was calculated to estimate the electronic level positions (Figure 4). The Fermi level differences between $CH_3NH_3PbI_3$ and TiO_2 build the driving force for the electron to transfer from the $CH_3NH_3PbI_3$ to the TiO_2 slab. Actually, a substantial amount of charge gather at the TiO_2 side due to the abrupt potential drop near the interface. Then, the built-in electric field in the interface hampers more electron transfer across the interface, and the electronic charge transfer equilibrium is reached. It is known that the built-in electric fields originate from the surface-surface interactions, particularly for the Pb^{2+} movement and the $CH_3NH_3^+$ orientation [58]. The incorporation of transition metals M ($M = Zn^{2+}$, Y^{3+}, Zr^{4+}, Nb^{5+}, Ru^{4+}, W^{6+}) enhances the polarization and the built-in electric field across the interfacial heterostructure. As shown in Figure 4, it is worth mentioning that the Zn- and Y-substituted interface models ($x = 10$Å) exhibit a substantial slope of electrostatic potential, while the others show the parameters' electrostatic potential. The potential drop in the Zn- and Y-substituted interfaces is notably steeper than that in the other interfaces, which serves as a reservoir for electrons. Hence, a substantial number of electrons gather at the TiO_2 surface, implying that the Zn^{2+} and Y^{3+} substituents are more efficient in separating the photo-generated electrons and holes.
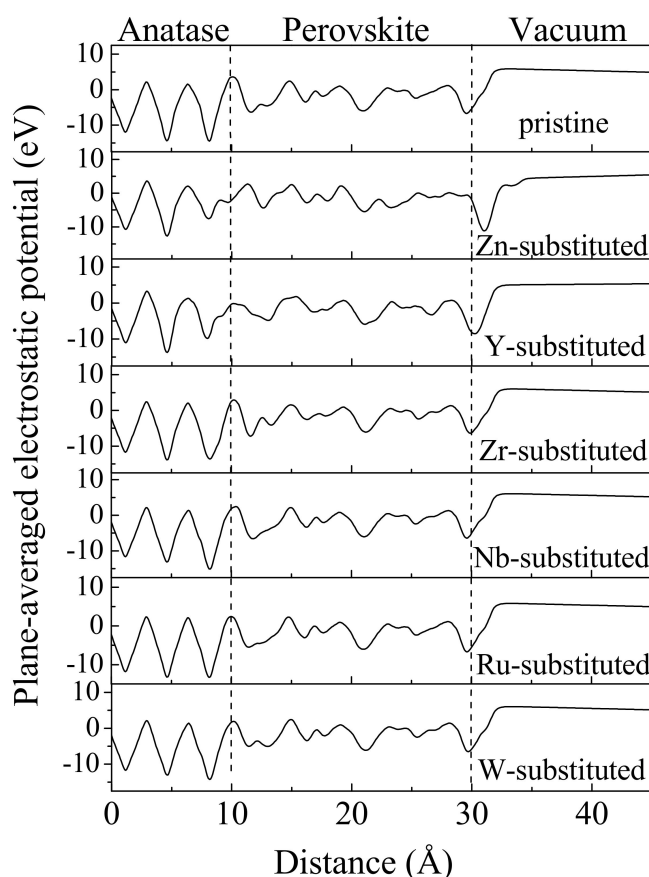

Figure 4. Planar averaged electrostatic potential across the optimized transition metal-substituted $CH_3NH_3PbI_3/TiO_2$.

To scrutinize the electronic property differences in various transition metal-substituted $CH_3NH_3PbI_3/TiO_2$, the bonding characteristics were analyzed by electron localization function (ELF), which can illustrate the type of bonding and delocalization of electron density in the interfacial system [59]. Figure 5 depicts the interfacial structures and ELF contour plots at (010) planes crossing the Pb^{2+} and I^- with color scheme for various interfacial systems. The ELF ranges from 0 to 1, where

red corresponds to a full localization, blue indicates a full delocalization, and green implies the uniform electron gas. The ELF slice exhibited lesser electron localization for the transition metal substituents than Ti^{4+}, which indicates a more covalent nature of the substituent-O interaction compared to the Ti–O interactions [60,61]. As can be seen, Figure 6a,d–g are quite similar, which explains why there is no variation in their geometry. By contrast, substitution with Zn^{2+} and Y^{3+} produced larger geometrical modification and electronic change in the $CH_3NH_3PbI_3/TiO_2$ interface. The ionic radius of transition metal substituents explains why there is no geometrical change with regard to the pristine and substituted systems. Compared with the Ti^{4+} cation (~0.6 Å) [62], the relatively large ionic radius of Y^{3+} (~0.9 Å) [63] and Zn^{2+} (~0.7 Å) [63] leads to distortions in the $CH_3NH_3PbI_3/TiO_2$ interface. Moreover, the binding energy and charge transfer analysis also led to the same conclusion. Interfacial bond strength varied with the ionic radius of transition metal in the substituted interfacial systems.
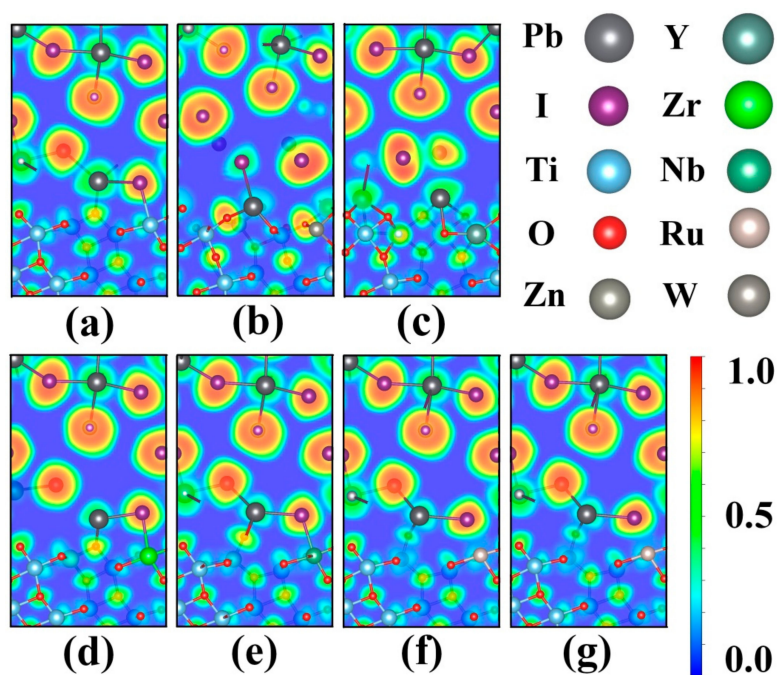

Figure 5. ELF of the optimized $CH_3NH_3PbI_3/TiO_2$ interfaces at (010) plane: (**a**) pristine, (**b**) Zn-substituted, (**c**) Y-substituted, (**d**) Zr-substituted, (**e**) Nb-substituted, (**f**) Ru-substituted, (**g**) W-substituted.
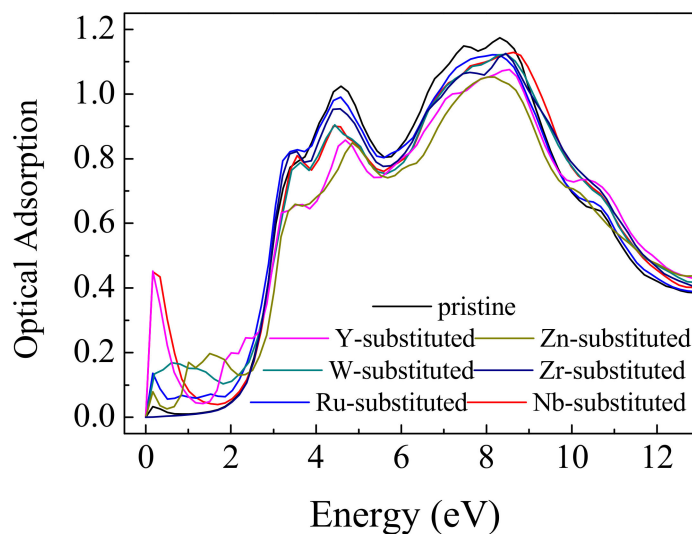

Figure 6. Comparison of the optical absorption of the transition metal-substituted $CH_3NH_3PbI_3/TiO_2$ interfaces.

The optical properties, including optical reflectivity, refractive index and absorption efficient can be obtained by dielectric function [64]. Taking into account that the PCE of $CH_3NH_3PbI_3$ mostly originates from the efficient use of visible light in the solar spectrum, only the calculated electronic absorption spectra of the $CH_3NH_3PbI_3/TiO_2$ interfaces have been investigated. The optical absorption coefficients (α) of different interfaces based on the obtained electronic structures are presented and compared in Figure 6. The absorption spectra parallel to *x*-axis were selected to examine the influence of transition metal substituents on the optical properties. The shapes of each absorption curve are close. As depicted in Figure 6, the $CH_3NH_3PbI_3/TiO_2$ interfaces have two absorption peaks—around 3.5 eV and 7.5 eV. The peak around 3.5 eV mainly comes from the conduction-to-valence band transition from I 5*p* or Pb 6*s* states to Pb 6*p* states [65]. On the other hand, the peak around 7.5 eV can be ascribed to the intrinsic band gap of pristine TiO_2 and the electron shifting from the O 2*p* to Ti 3*d* orbitals [66]. It has also been reported that the absorption of pure TiO_2 is limited to ultraviolet (UV) light and exhibits inefficient response for visible light. In case of the pristine $CH_3NH_3PbI_3/TiO_2$, our theoretical calculation is consistent with the experimental values and theoretical studies [67,68]. In case of the substituted $CH_3NH_3PbI_3/TiO_2$, the substituted interface still shows poor photoactivity in the visible-light region for solar light harvesting. However, it has an extra absorption peak in the low energy region (less than 2 eV). The incorporation of the transition metal substituents into the $CH_3NH_3PbI_3/TiO_2$ interface leads to an obvious red-shift effect. The distinct absorption peak at 0.3 eV in the low energy region can be attributed to the band gap near the Fermi level. The decrease in intensity of transition energies is caused by the split intra-band transitions between the impurity states, rendering the more obvious red-shift [68]. Compared with the pristine $CH_3NH_3PbI_3/TiO_2$ interface, the transition metal-substituted $CH_3NH_3PbI_3/TiO_2$ interface is expected to be more active for efficient visible-light photo-catalysis.

In order to further elucidate the charge carrier separation mechanism of the $CH_3NH_3PbI_3/TiO_2$ interfaces, partial density of states (PDOS) have been calculated for pure and substituted $CH_3NH_3PbI_3/TiO_2$ interfaces. As seen in Figure 7, the PDOS is split into contributions from $CH_3NH_3PbI_3$, TiO_2 and transition metal substituents. The substituent component is magnified five times for better visibility. It is already known that the band gap of TiO_2 is wider than that of the $CH_3NH_3PbI_3$ perovskite [25,26]. Besides, the conduction band minimum (CBM) of TiO_2 is lower than that of $CH_3NH_3PbI_3$. They can excite electrons from the valence band of $CH_3NH_3PbI_3$ (I 5*p* and Pb 6*s* orbitals) to conduction band of $CH_3NH_3PbI_3$ (Pb 6*p*), and then transfer to conduction band of TiO_2 (Ti 3*d*). The difference between Pb 6*p* and Ti 3*d* decided the efficiency of charge transfer across the interface [69]. The interfacial band gaps can be tuned by n, p, and isovalent substituents using the selected transition metals. As shown in Figure 7, n substitution agents such as Nb^{5+} and W^{6+} pushed the Fermi level into the conduction band and made the system metallic. The intensity of the Fermi levels entering into the conduction band should be increased as the *d* states of substituents changes from 4*d* to 5*d* transition metals. By contrast, in the p substitution agents (Zn^{2+} and Y^{3+}) modified interfaces, the Fermi levels shifted from valence band to conduction band, leading to obvious band gaps compared with the pristine system. For the isovalent substituted (Zr^{4+}, Ru^{4+}) interfaces, the PDOS shape of substituted interface is wider than that of the pristine interface, which implies that the electronic nonlocality becomes quite obvious. The delocalized transition metal *d* state contributes to the electron–hole pair separation in the PSC and supports carrier migration within the photo-catalysis process.

Schematic diagrams of the energy levels of various elements' substitution TiO_2 are shown in Figure 8. The vacuum level of the system was set to 0 eV for comparison. The CBM of pristine TiO_2 was found to be located at −4.1 eV. It can be seen that the substituent ion effectively modified the CBM state of the TiO_2. In all the cases, the CBM gradually up-shifts to the vacuum level as the substituent change from n to p. The Fermi level shifts downward with p substituent and the electron injection from perovskite to p substituted TiO_2 will be hindered. On the other hand, the optimal band alignment between perovskite and n substituted TiO_2 could effectively improve the charge transport and suppress charge recombination. From this point of view, Nb^{5+} and W^{6+} substituted interfaces are expected to

have better device performance. Tuning energy level alignment by element substitution ($M = Zn^{2+}$, Y^{3+}, Zr^{4+}, Nb^{5+}, Ru^{4+}, W^{6+}) is confirmed to be an effective way to optimize charge transportation and thus enhance the PCE of PSC.
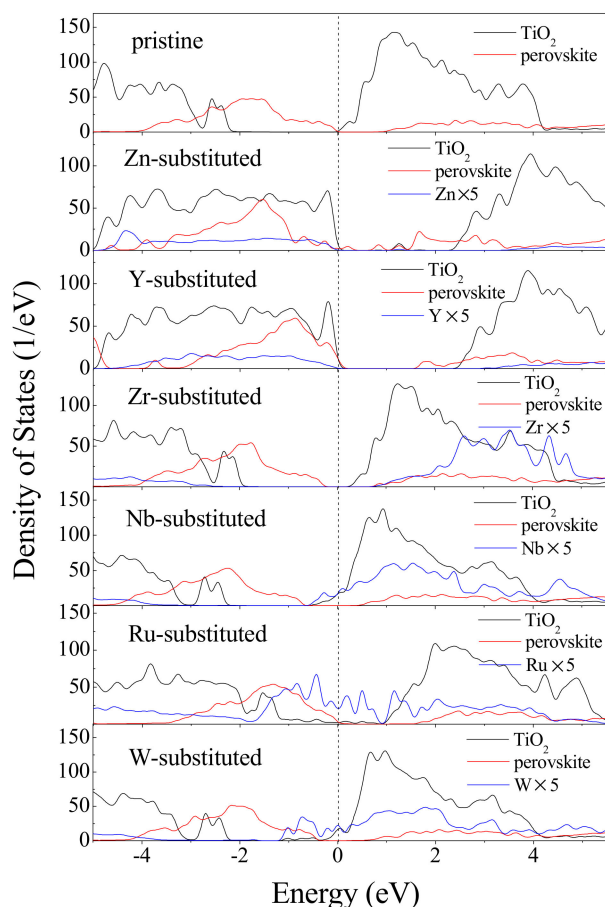

Figure 7. DOS of pristine and transition metal-substituted $CH_3NH_3PbI_3/TiO_2$ interface.
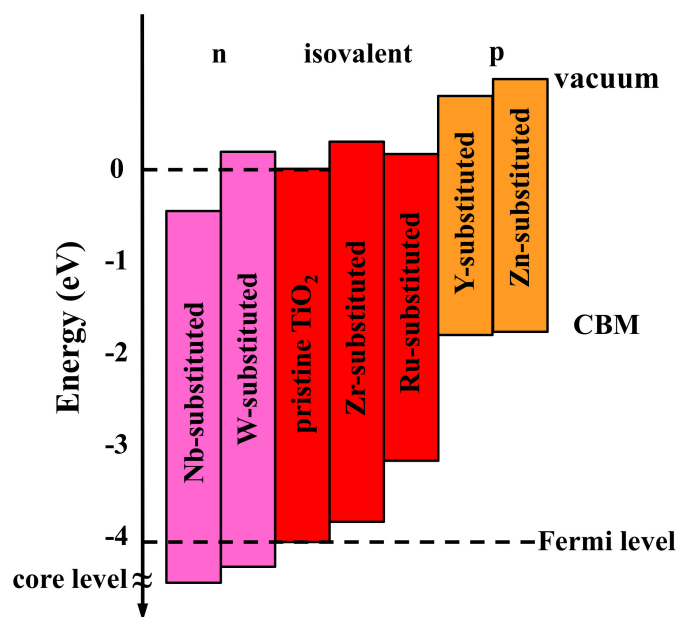

Figure 8. Schematic energy level diagram of element substituted TiO_2.

4. Concluding Remarks

First-principles computations were utilized to characterize the structural, electronic and optical properties of the transition metal-substituted $CH_3NH_3PbI_3/TiO_2$ interface. Through density functional calculations for binding energy and charge transfer of various configurations, we found that the substitution of Ti^{4+} at the Ti_{5c} sites by transition metals is energetically favored. Especially, the p dopings of Zn^{2+} and Y^{3+} for Ti^{4+} at interfaces are the most energetically favorable among the transition metals, which lead to improved interfacial stability. Electrostatic potential investigations revealed that the potential drop in the Zn- and Y-substituted interfaces is notably steeper than that in the other interfaces, indicating that the substituents are more efficient in separating the carriers. The relatively large ionic radius of Y^{3+} and small ionic radius of Zn^{2+} lead to distortions in the ELF calculations. The calculated absorption spectra indicate that the transition metal-substituted $CH_3NH_3PbI_3/TiO_2$ interface retains an enhanced visible light photocatalytic ability owing to the decreased transition energies. Closer comparisons between pristine and substituted $CH_3NH_3PbI_3/TiO_2$ indicate that the interfacial band gaps can be tuned by n, p, and isovalent substituents using the selected transition metals. Due to their optimal band alignment, the Nb^{5+} and W^{6+} substituted interface have better device performance. Theoretical studies predict that the varied mechanisms depending on transition metal substations will exert different effects on properties of $CH_3NH_3PbI_3/TiO_2$ interfaces. Our calculations explain why transition metals M ($M = Zn^{2+}$, Y^{3+}, Zr^{4+}, Nb^{5+}, Ru^{4+}, W^{6+}) could enhance device performance and why it is helpful for the potential commercialization of planar heterojunction PSC.

References

1. Chen, J.; Zhou, S.; Jin, S.; Li, H.; Zhai, T. Crystal Organometal Halide Perovskites with Promising Optoelectronic Applications. *J. Mater. Chem. C* **2016**, *4*, 11–27. [CrossRef]

2. Yang, M.; Li, Z.; Reese, M.O.; Reid, O.G.; Kim, D.H.; Siol, S.; Klein, T.R.; Yan, Y.; Berry, J.J.; van Hest, M.F.A.M.; et al. Perovskite Ink with Wide Processing Window for Scalable High-Efficiency Solar Cells. *Nat. Energy* **2017**, *2*, 17038.

3. Chen, W.; Wu, Y.; Yue, Y.; Liu, J.; Zhang, W.; Yang, X.; Chen, H.; Bi, E.; Ashraful, I.; Grätzel, M.; et al. Efficient and Stable Large-Area Perovskite Solar Cells with Inorganic Charge Extraction Layers. *Science* **2015**, *350*, 944–948. [CrossRef] [PubMed]

4. Heo, J.H.; Han, H.J.; Kim, D.; Ahn, T.K.; Im, S.H. Hysteresis-Less Inverted $CH_3NH_3PbI_3$ Planar Perovskite Hybrid Solar Cells with 18.1% Power Conversion Efficiency. *Energy Environ. Sci.* **2015**, *8*, 1602–1608. [CrossRef]

5. Lu, Z.; Wang, S.; Liu, H.; Feng, F.; Li, W. Improved Efficiency of Perovskite Solar Cells by the Interfacial Modification of the Active Layer. *Nanomaterials* **2019**, *9*, 204. [CrossRef] [PubMed]

6. Mohamad Noh, M.F.; Teh, C.H.; Daik, R.; Lim, E.L.; Yap, C.C.; Ibrahim, M.A.; Ahmad Ludin, N.; Mohd Yusoff, A.R.b.; Jang, J.; Mat Teridi, M.A. The Architecture of the Electron Transport Layer for a Perovskite Solar Cell. *J. Mater. Chem. C* **2018**, *6*, 682–712. [CrossRef]

7. Yang, G.; Tao, H.; Qin, P.; Ke, W.; Fang, G. Recent Progress in Electron Transport Layers for Efficient Perovskite Solar Cells. *J. Mater. Chem. A* **2016**, *4*, 3970–3990. [CrossRef]

8. Ke, W.; Fang, G.; Liu, Q.; Xiong, L.; Qin, P.; Tao, H.; Wang, J.; Lei, H.; Li, B.; Wan, J.; et al. Low-Temperature Solution-Processed Tin Oxide as an Alternative Electron Transporting Layer for Efficient Perovskite Solar Cells. *J. Am. Chem. Soc.* **2015**, *137*, 6730–6733. [CrossRef]

9.   Yang, H.-Y.; Rho, W.-Y.; Lee, S.K.; Kim, S.H.; Hahn, Y.-B. TiO$_2$ Nanoparticles/Nanotubes for Efficient Light Harvesting in Perovskite Solar Cells. *Nanomaterials* **2019**, *9*, 326. [CrossRef]

10.   Lindblad, R.; Bi, D.; Park, B.-W.; Oscarsson, J.; Gorgoi, M.; Siegbahn, H.; Odelius, M.; Johansson, E.M.J.; Rensmo, H. Electronic Structure of TiO$_2$/CH$_3$NH$_3$PbI$_3$ Perovskite Solar Cell Interfaces. *J. Phys. Chem. Lett.* **2014**, *5*, 648–653. [CrossRef]

11.   Yella, A.; Heiniger, L.-P.; Gao, P.; Nazeeruddin, M.K.; Grätzel, M. Nanocrystalline Rutile Electron Extraction Layer Enables Low-Temperature Solution Processed Perovskite Photovoltaics with 13.7% Efficiency. *Nano Lett.* **2014**, *14*, 2591–2596. [CrossRef] [PubMed]

12.   Gao, X.-X.; Ge, Q.-Q.; Xue, D.-J.; Ding, J.; Ma, J.-Y.; Chen, Y.-X.; Zhang, B.; Feng, Y.; Wan, L.-J.; Hu, J.-S. Tuning the Fermi-Level of TiO$_2$ Mesoporous Layer by Lanthanum Doping towards Efficient Perovskite Solar Cells. *Nanoscale* **2016**, *8*, 16881–16885. [CrossRef] [PubMed]

13.   Yin, G.; Ma, J.; Jiang, H.; Li, J.; Yang, D.; Gao, F.; Zeng, J.; Liu, Z.; Liu, S.F. Correction to Enhancing Efficiency and Stability of Perovskite Solar Cells through Nb-Doping of TiO$_2$ at Low Temperature. *Acs Appl. Mater. Interfaces* **2017**, *9*, 14545. [CrossRef] [PubMed]

14.   Chen, B.-X.; Rao, H.-S.; Li, W.-G.; Xu, Y.-F.; Chen, H.-Y.; Kuang, D.-B.; Su, C.-Y. Achieving High-Performance Planar Perovskite Solar Cell with Nb-Doped TiO$_2$ Compact Layer by Enhanced Electron Injection and Efficient Charge Extraction. *J. Mater. Chem. A* **2016**, *4*, 5647–5653. [CrossRef]

15.   Chen, S.-H.; Chan, S.-H.; Lin, Y.-T.; Wu, M.-C. Enhanced Power Conversion Efficiency of Perovskite Solar Cells Based on Mesoscopic Ag-Doped TiO$_2$ Electron Transport Layer. *Appl. Surf. Sci.* **2019**, *469*, 18–26. [CrossRef]

16.   Liu, D.; Li, S.; Zhang, P.; Wang, Y.; Zhang, R.; Sarvari, H.; Wang, F.; Wu, J.; Wang, Z.; Chen, Z.D. Efficient Planar Heterojunction Perovskite Solar Cells with Li-Doped Compact TiO$_2$ Layer. *Nano Energy* **2017**, *31*, 462–468. [CrossRef]

17.   Wu, M.-C.; Chan, S.-H.; Jao, M.-H.; Su, W.-F. Enhanced Short-Circuit Current Density of Perovskite Solar Cells Using Zn-Doped TiO$_2$ as Electron Transport Layer. *Sol. Energy Mater. Sol. Cells* **2016**, *157*, 447–453. [CrossRef]

18.   Xu, Z.; Yin, X.; Guo, Y.; Pu, Y.; He, M. Ru-Doping in TiO$_2$ Electron Transport Layers of Planar Heterojunction Perovskite Solar Cells for Enhanced Performance. *J. Mater. Chem. C* **2018**, *6*, 4746–4752. [CrossRef]

19.   Liu, J.; Zhang, J.; Yue, G.; Lu, X.; Hu, Z.; Zhu, Y. W-Doped TiO$_2$ Photoanode for High Performance Perovskite Solar Cell. *Electrochim. Acta* **2016**, *195*, 143–149.

20.   Zhou, H.; Chen, Q.; Li, G.; Luo, S.; Song, T.-B.; Duan, H.-S.; Hong, Z.; You, J.; Liu, Y.; Yang, Y. Interface Engineering of Highly Efficient Perovskite Solar Cells. *Science* **2014**, *345*, 542–546. [CrossRef]

21.   Cui, Q.; Zhao, X.; Lin, H.; Yang, L.; Chen, H.; Zhang, Y.; Li, X. Improved Efficient Perovskite Solar Cells Based on Ta-Doped TiO$_2$ Nanorod Arrays. *Nanoscale* **2017**, *9*, 18897–18907. [CrossRef] [PubMed]

22.   García-Mota, M.; Vojvodic, A.; Abild-Pedersen, F.; Nørskov, J.K. Electronic Origin of the Surface Reactivity of Transition-Metal-Doped TiO$_2$(110). *J. Phys. Chem. C* **2013**, *117*, 460–465. [CrossRef]

23.   Pathak, S.K.; Abate, A.; Ruckdeschel, P.; Roose, B.; Gödel, K.C.; Vaynzof, Y.; Santhala, A.; Watanabe, S.-I.; Hollman, D.J.; Noel, N.; et al. Performance and Stability Enhancement of Dye-Sensitized and Perovskite Solar Cells by Al Doping of TiO$_2$. *Adv. Funct. Mater.* **2014**, *24*, 6046–6055. [CrossRef]

24.   Xu, X.; Li, K.; Yang, Z.; Shi, J.; Li, D.; Gu, L.; Wu, Z.; Meng, Q. Methylammonium Cation Deficient Surface for Enhanced Binding Stability at TiO$_2$/CH$_3$NH$_3$PbI$_3$ Interface. *Nano Res.* **2017**, *10*, 483–490. [CrossRef]

25.   Geng, W.; Tong, C.-J.; Liu, J.; Zhu, W.; Lau, W.-M.; Liu, L.-M. Structures and Electronic Properties of Different CH$_3$NH$_3$PbI$_3$/TiO$_2$ Interface: A First-Principles Study. *Sci. Rep.* **2016**, *6*, 20131. [CrossRef] [PubMed]

26.   Ji, G.; Zheng, G.; Zhao, B.; Song, F.; Zhang, X.; Shen, K.; Yang, Y.; Xiong, Y.; Gao, X.; Cao, L.; et al. Interfacial Electronic Structures Revealed at the Rubrene/CH$_3$NH$_3$PbI$_3$ Interface. *Phys. Chem. Chem. Phys.* **2017**, *19*, 6546–6553. [CrossRef] [PubMed]

27.   Feng, H.-J. Ferroelectric Polarization Driven Optical Absorption and Charge Carrier Transport in CH$_3$NH$_3$PbI$_3$/TiO$_2$-Based Photovoltaic Cells. *J. Power Sources* **2015**, *291*, 58–65. [CrossRef]

28.   Hu, J.; Ji, G.; Ma, X.; He, H.; Huang, C. Probing Interfacial Electronic Properties of Graphene/CH$_3$NH$_3$PbI$_3$ Heterojunctions: A Theoretical Study. *Appl. Surf. Sci.* **2018**, *440*, 35–41. [CrossRef]

29.   Nemnes, G.A.; Goehry, C.; Mitran, T.L.; Nicolaev, A.; Ion, L.; Antohe, S.; Plugaru, N.; Manolescu, A. Band Alignment and Charge Transfer in Rutile-TiO$_2$/CH$_3$NH$_3$PbI$_{3-x}$Cl$_x$ Interfaces. *Phys. Chem. Chem. Phys.* **2015**, *17*, 30417–30423. [CrossRef]

30. Haruyama, J.; Sodeyama, K.; Hamada, I.; Han, L.; Tateyama, Y. First-Principles Study of Electron Injection and Defects at the $TiO_2/CH_3NH_3PbI_3$ Interface of Perovskite Solar Cells. *J. Phys. Chem. Lett.* **2017**, *8*, 5840–5847. [CrossRef]

31. Mosconi, E.; Grancini, G.; Roldán-Carmona, C.; Gratia, P.; Zimmermann, I.; Nazeeruddin, M.K.; De Angelis, F. Enhanced TiO_2/MAPbI$_3$ Electronic Coupling by Interface Modification with PbI_2. *Chem. Mater.* **2016**, *28*, 3612–3615.

32. Kresse, G.; Furthmüller, J. Efficiency of Ab-initio Total Energy Calculations for Metals and Semiconductors Using a Plane-Wave Basis Set. *Comput. Mater. Sci.* **1996**, *6*, 15–50.

33. Blöchl, P.E. Projector Augmented-Wave Method. *Phys. Rev. B* **1994**, *50*, 17953. [CrossRef] [PubMed]

34. Zhang, Y.; Yang, W. Generalized Gradient Approximation Made Simple. *Phys. Rev. Lett.* **1996**, *77*, 3865.

35. Monkhorst, H.J.; Pack, J.D. Special Points for Brillouin-Zone Integrations. *Phys. Rev. B* **1976**, *13*, 5188. [CrossRef]

36. Mosconi, E.; Umari, P.; De Angelis, F. Electronic and Optical Properties of MAPbX$_3$ Perovskites (X = I, Br, Cl): A Unified DFT and GW Theoretical Analysis. *Phys. Chem. Chem. Phys.* **2016**, *18*, 27158–27164. [CrossRef] [PubMed]

37. Sumita, M.; Sodeyama, K.; Jono, R.; Han, L.; Tateyama, Y. Electronic Structure of Acetonitrile Adsorbed on the Anatase TiO_2 (101) Surface. *Chem. Phys. Lett.* **2013**, *556*, 225–229.

38. Sun, R.; Wang, Z.; Shibata, N.; Ikuhara, Y. A Dislocation Core in Titanium Dioxide and Its Electronic Structure. *Rsc Adv.* **2015**, *5*, 18506–18510. [CrossRef]

39. Fang, Y.; Cheng, D.; Niu, M.; Yi, Y.; Wu, W. Tailoring the Electronic and Optical Properties of Rutile TiO_2 by (Nb+Sb, C) Codoping from DFT+U Calculations. *Chem. Phys. Lett.* **2013**, *567*, 34–38.

40. Hou, Y.S.; Xiang, H.J.; Gong, X.G. Unveiling Magnetic Interactions of Ruthenium Trichloride via Constraining Direction of Orbital Moments: Potential Routes to Realize a Quantum Spin Liquid. *Phys. Rev. B* **2017**, *96*, 054410. [CrossRef]

41. Gong, J.; Yang, C.; Zhang, J.; Pu, W. Origin of photocatalytic activity of W/N-codoped TiO_2:H$_2$ production and DFT calculation with GGA+U. *Appl. Catal. B Environ.* **2014**, *152–153*, 73–81. [CrossRef]

42. Zasada, F.; Gryboś, J.; Indyka, P.; Piskorz, W.; Kaczmarczyk, J.; Sojka, Z. Surface Structure and Morphology of M[CoM']O$_4$ (M = Mg, Zn, Fe, Co and M' = Ni, Al, Mn, Co) Spinel Nanocrystals—DFT+U and TEM Screening Investigations. *J. Phys. Chem. C* **2014**, *118*, 19085–19097. [CrossRef]

43. Chen, H.-Y.T.; Tosoni, S.; Pacchioni, G. Adsorption of Ruthenium Atoms and Clusters on Anatase TiO_2 and Tetragonal ZrO_2(101) Surfaces: A Comparative DFT Study. *J. Phys. Chem. C* **2015**, *119*, 10856–10868. [CrossRef]

44. Methfessel, M.; Paxton, A.T. High-Precision Sampling for Brillouin-Zone Integration in Metals. *Phys. Rev. B* **1989**, *40*, 3616–3621. [CrossRef] [PubMed]

45. Even, J.; Pedesseau, L.; Jancu, J.-M.; Katan, C. Importance of Spin–Orbit Coupling in Hybrid Organic/Inorganic Perovskites for Photovoltaic Applications. *J. Phys. Chem. Lett.* **2013**, *4*, 2999–3005. [CrossRef]

46. Momma, K.; Izumi, F. VESTA: A Three-Dimensional Visualization System for Electronic and Structural Analysis. *J. Appl. Crystallogr.* **2008**, *41*, 653–658. [CrossRef]

47. Ke, W.; Fang, G.; Wang, J.; Qin, P.; Tao, H.; Lei, H.; Liu, Q.; Dai, X.; Zhao, X. Perovskite Solar Cell with an Efficient TiO_2 Compact Film. *Acs Appl. Mater. Interfaces* **2014**, *6*, 15959–15965. [CrossRef] [PubMed]

48. Mosconi, E.; Ronca, E.; De Angelis, F. First-Principles Investigation of the TiO_2/Organohalide Perovskites Interface: The Role of Interfacial Chlorine. *J. Phys. Chem. Lett.* **2014**, *5*, 2619–2625. [CrossRef]

49. Li, Z.; Wang, X.; Chi, B. First Principles Investigation of the Conversion of N_2O and CO to N_2 and CO_2 on a Modified N + Fe/TiO_2 (101) Surface. *Rsc Adv.* **2014**, *4*, 17896–17901. [CrossRef]

50. Chen, Q.L.; Li, B.; Zheng, G.; He, K.H.; Zheng, A.S. First-Principles Calculations on Electronic Structures of Fe-Vacancy-Codoped TiO_2 Anatase (101) Surface. *Phys. B Condens. Matter* **2011**, *406*, 3841–3846. [CrossRef]

51. Ma, J.-G.; Zhang, C.-R.; Gong, J.-J.; Wu, Y.-Z.; Kou, S.-Z.; Yang, H.; Chen, Y.-H.; Liu, Z.-J.; Chen, H.-S. The Electronic Structures and Optical Properties of Alkaline-Earth Metals Doped Anatase TiO_2: A Comparative Study of Screened Hybrid Functional and Generalized Gradient Approximation. *Materials* **2015**, *8*, 5508–5525. [CrossRef] [PubMed]

52. Cromer, D.T.; Herrington, K. The Structures of Anatase and Rutile. *J. Am. Chem. Soc.* **1955**, *77*, 4708–4709. [CrossRef]

53. Feng, J.; Xiao, B. Crystal Structures, Optical Properties, and Effective Mass Tensors of $CH_3NH_3PbX_3$ (X = I and Br) Phases Predicted from HSE06. *J. Phys. Chem. Lett.* **2014**, *5*, 1278–1282. [CrossRef] [PubMed]

54. Kawamura, Y.; Mashiyama, H.; Hasebe, K. Structural Study on Cubic-Tetragonal Transition of $CH_3NH_3PbI_3$. *J. Phys. Soc. Jpn.* **2002**, *71*, 1694–1697. [CrossRef]

55. Yang, Z.; Wang, Y.; Liu, Y. Stability and Charge Separation of Different $CH_3NH_3SnI_3/TiO_2$ Interface: A First-Principles Study. *Appl. Surf. Sci.* **2018**, *441*, 394–400. [CrossRef]

56. Si, F.; Hu, W.; Tang, F.; Cheng, Y.; Xue, H. Electronic and Optical Properties of the Wurtzite- $ZnO/CH_3NH_3PbI_3$ Interface: First-Principles Calculations. *J. Mater. Sci.* **2017**, *52*, 13841–13851. [CrossRef]

57. Henkelman, G.; Arnaldsson, A.; Jónsson, H. A Fast and Robust Algorithm for Bader Decomposition of Charge Density. *Comput. Mater. Sci.* **2006**, *36*, 354–360.

58. Feng, H.-J.; Paudel, T.R.; Tsymbal, E.Y.; Zeng, X.C. Tunable Optical Properties and Charge Separation in $CH_3NH_3Sn_xPb_{1−x}I_3/TiO_2$-Based Planar Perovskites Cells. *J. Am. Chem. Soc.* **2015**, *137*, 8227–8236. [CrossRef]

59. Liu, R.; Zhou, X.; Yang, F.; Yu, Y. Combination Study of DFT Calculation and Experiment for Photocatalytic Properties of S-Doped Anatase TiO_2. *Appl. Surf. Sci.* **2014**, *319*, 50–59. [CrossRef]

60. Navas, J.; Sánchez-Coronilla, A.; Aguilar, T.; Hernández, N.C.; de los Santos, D.M.; Sánchez-Márquez, J.; Zorrilla, D.; Fernández-Lorenzo, C.; Alcántara, R.; Martín-Calleja, J. Experimental and theoretical study of the electronic properties of Cu-doped anatase TiO_2. *Phys. Chem. Chem. Phys.* **2014**, *16*, 3835–3845. [CrossRef]

61. Navas, J.; Sánchez-Coronilla, A.; Gallardo, J.J.; Cruz Hernández, N.; Piñero, J.C.; Alcántara, R.; Fernández-Lorenzo, C.; De los Santos, D.M.; Aguilar, T.; Martín-Calleja, J. New Insights into Organic–Inorganic Hybrid Perovskite $CH_3NH_3PbI_3$ Nanoparticles. An Experimental and Theoretical Study of Doping in Pb^{2+} Sites with Sn^{2+}, Sr^{2+}, Cd^{2+} and Ca^{2+}. *Nanoscale* **2015**, *7*, 6216–6229. [CrossRef] [PubMed]

62. Li, R.-W.; Wang, Z.-H.; Chen, X.; Sun, J.-R.; Shen, B.-G. Magnetic Properties and Colossal Magnetoresistance of the Perovskites $La_{2/3}Ca_{1/3}Mn_{1−x}Ti_xO$. *J. Appl. Phys.* **2000**, *87*, 5597–5599. [CrossRef]

63. Liu, J.; Wang, Y.; Yu, X.; Li, J. Enhanced Photoluminescence Properties of $Zn_2SiO_4:Mn^{2+}$ Co-Activated with Y^{3+}/Li^+ under VUV Excitation. *J. Lumin.* **2010**, *130*, 2171–2174. [CrossRef]

64. Yang, J.Y.; Liu, L.H.; Tan, J.Y. First-principles Molecular Dynamics Study on Temperature-Dependent Dielectric Function of Bulk 3C and 6H SiC in the Energy Range 3–8eV. *Phys. B Condens. Matter* **2014**, *436*, 182–187. [CrossRef]

65. Lin, C.; Li, S.; Zhang, W.; Shao, C.; Yang, Z. Effect of Bromine Substitution on the Ion Migration and Optical Absorption in $MAPbI_3$ Perovskite Solar Cells: The First-Principles Study. *Acs Appl. Energy Mater.* **2018**, *1*, 1374–1380. [CrossRef]

66. Khan, M.; Xu, J.; Chen, N.; Cao, W. First Principle Calculations of the Electronic and Optical Properties of Pure and (Mo, N) Co-Doped Anatase TiO_2. *J. Alloy. Compd.* **2012**, *513*, 539–545. [CrossRef]

67. Dashora, A.; Patel, N.; Kothari, D.C.; Ahuja, B.L.; Miotello, A. Formation of an Intermediate Band in the Energy Gap of TiO_2 by Cu–N-Codoping: First Principles Study and Experimental Evidence. *Sol. Energy Mater. Sol. Cells* **2014**, *125*, 120–126. [CrossRef]

68. Jia, L.; Wu, C.; Han, S.; Yao, N.; Li, Y.; Li, Z.; Chi, B.; Pu, J.; Jian, L. Theoretical Study on the Electronic and Optical Properties of (N, Fe)-Codoped Anatase TiO_2 Photocatalyst. *J. Alloy. Compd.* **2011**, *509*, 6067–6071. [CrossRef]

69. Long, R.; Prezhdo, O.V. Dopants Control Electron–Hole Recombination at Perovskite-TiO_2 Interfaces: Ab Initio Time-Domain Study. *ACS Nano* **2015**, *9*, 11143–11155. [CrossRef]